Mapping Surface Deformation Over Tatun Volcano Group, Northern Taiwan Using Multitemporal InSAR

Hongyu Liang, *Member, IEEE*, Xin Li, and Rou-Fei Chen

***Abstract*—The Tatun Volcano Group (TVG) is located at the northern coast of Taiwan Island with only 15 km to the Taipei metropolis. Recent geothermal and geochemical studies suggest that the TVG is dormant-active rather than extinct, implying the eruption potential to devastate the nearby area of 7 million inhabitants. Although some geodetic tools (e.g., global positioning system and precise leveling) have been utilized to analyze the activity associated with volcanism, it is still challenging for conventional interferometric synthetic aperture radar (InSAR) technique to obtain clear ground surface movement at the TVG due to decorrelation and complex atmospheric delay. In this study, we present an improved multi-temporal InSAR (MTInSAR) approach to explore the temporal evolution and spatial extent of displacement at the TVG from 19 L-band ALOS/PALSAR images acquired between 2007 and 2011. Stratified atmospheric delays and orbit error are corrected with a patch-based joint model as different phase components can be separated according to their distinct spatiotemporal characteristics. The spatial deformation patterns indicate an uplift of 10 mm/year at the SW-NE ridge and subsidence with a rate of 10 mm/year at the E-W ridge. The temporal deformation variations at Mt. Chihshin and Huangzuei have high similarity with correlation coefficients of 0.9 above. This indicates that the subsidence at Mts. Chihshin and Huangzuei might be caused by released hydrothermal fluids related to tectono-magmatic activity within the hydrothermal system beneath the TVG.**

***Index Terms*—Interferometric synthetic aperture radar (InSAR), orbital error, Tatun Volcano Group (TVG), tropospheric delay.**

I. Introduction

THE Tatun Volcano Group (TVG) is located at the northern tip of Taiwan adjacent to two metropolises (i.e., Taipei city and New Taipei city). As the result of subduction of the Philippine Sea plate beneath the Eurasian plate [1], [2], the TVG covers an area of 400 km^2 with more than 20 quaternary volcanoes. Among them, Mts. Chihshin and Huangzuei are known to have produced magmatic eruptions between about 23 000 and 13 000 years ago [3], [4]. Although from the general identification of active volcanoes [5], the TVG has been classified as an extinct volcano group, and some volcano subgroups thereof (e.g., Mt. Chihshin) have been proven to be potentially active according to recent geophysical and geochemical observations [6]−[8]. Considering 7 million inhabitants and two nuclear power plants are distributed in the vicinity of the TVG, any volcanic activity may have a significant impact on the surrounding area. Understanding the dynamic nature of volcanic activity at the TVG is not only a fundamental scientific issue but also a societal need to mitigate damages from the possible eruptions.

Investigating the volcanic activity at the TVG involves multidisciplinary efforts that have been dedicated to detecting the early sign of unrest and assessing associated geohazards. Based on the analysis of volcaniclastic deposits and lava flows, the geological and geomorphological studies suggest that the last Plinian eruption may have happened at a period from 23 000 to 13 000 years ago, and a phreatic explosion at the TVG may have occurred approximately 6000 years ago [4]. Observations from the TVG seismic network have been used to detect volcanic earthquakes and tremors which often relate to the magma reservoir [8]−[10]. The seismic waves observed between 2003 and 2016 indicate that a deep magma reservoir might exist beneath the TVG with a total volume of approximately 350−936 km^3 upon the level of partial melting [7]. Geochemical monitoring from the composition of fumarolic gases and hot springs also shows that the strong fumarolic activities originate from the magma source beneath the TVG [6], [11], [12].

In addition to the geophysical and geochemical studies, it is reported that the ground surface movement can reveal the underlying volcanic activities, such as volcanic eruption and volcanic unrest [13], [14]. However, *in situ* or ground-based observations from, e.g., global positioning system (GPS) and sprite leveling [15], [16], are inadequate to reveal the detailed surface deformation, limiting the capability in constraining the geometry of magma source underneath. Interferometric synthetic aperture radar (InSAR) provides a remote-sensed way to explore the ground movement with large spatial coverage, high spatial resolution, and satisfactory accuracy. This technique has demonstrated its effectiveness in mapping crustal deformation associated with earthquakes [17], glacier motion [18], landslides [19], underground withdrawal [20], etc. However, the dense vegetation at the TVG poses a challenge for conventional InSAR

Manuscript received March 30, 2020; revised November 29, 2020; accepted January 1, 2021. Date of publication January 13, 2021; date of current version February 3, 2021. This work was supported in part by the China Postdoctoral Science Foundation under Grant 2019M650830, in part by National Natural Science Foundation of China under Grant 41774023 and Grant 41304011, in part by Research Grants Council of Hong Kong under Grant PolyU152232/17E and Grant PolyU152164/18E, and in part by Grant MOST108-2116-M-034-004. *(Corresponding author: Xin Li.)*

Hongyu Liang is with the College of Surveying and Geo-Informatics, Tongji University, Shanghai 200092, China (e-mail: allenhongyu.liang@connect.polyu.hk).

Xin Li is with the State Key Laboratory of Resources and Environmental Information System, Institute of Geographic Sciences and Natural Resources Research, Chinese Academy of Sciences, Beijing 100049, China (e-mail: vivianyoxi@gmail.com).

Rou-Fei Chen is with the Department of Materials and Mineral Resources Engineering, National Taipei University of Technology, Taipei 10608, Taiwan (e-mail: roufei@earth.sinica.edu.tw).

Digital Object Identifier 10.1109/JSTARS.2021.3050644

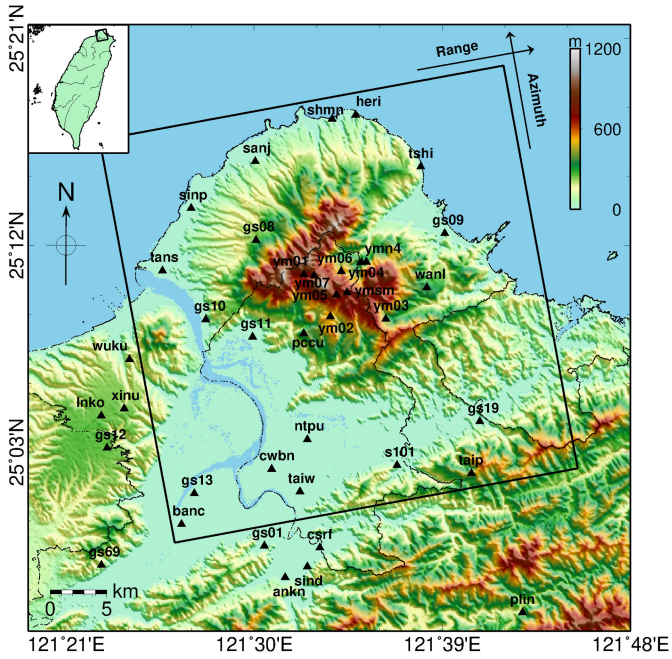

Fig. 1. Topographic map of Taipei Basin generated from SRTM data. The black solid box outlines the study area covered by ALOS/PALSAR images used (track 444, frame 490). The black triangles represent the GPS sites.

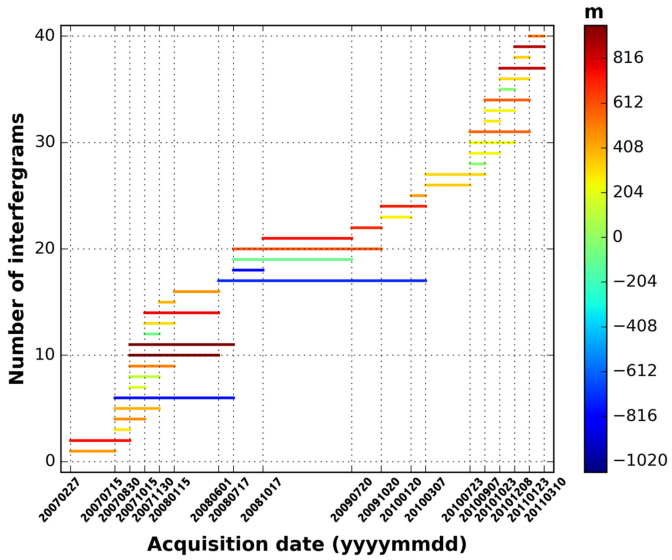

Fig. 2. Spatial and temporal baselines of selected interferometric pairs which are represented by color and length of line, respectively.

techniques to extract the detailed spatial extent of deformation [21]. Other error sources of InSAR measurements at the TVG, like tropospheric delay and topographic inaccuracy, are strong, obscuring the retrieval of accurate deformation information.

In this study, we adopt an enhanced multitemporal InSAR (MTInSAR) approach to explore the temporal evolution and spatial extent of deformation at the TVG from 19 descending ALOS/PALSAR images. In this approach, stratified atmospheric delays and orbit errors are corrected by a patch-based joint method. The derived time-series displacements are quantitatively validated by *in situ* GPS measurements. The results allow us to gain better understanding of the volcanic-hydrothermal dynamics beneath the TVG. It also demonstrates the capability of InSAR technology to monitor the underlying activities at volcanic zones even covered by heavy vegetation and with complicated atmospheric distortions.

II. Methodology

A. Data Preprocessing

In this study, we use 19 descending ALOS/PALSAR images acquired from February 2007 to March 2011 to analyze the time-series displacements at the TVG. The cropped coverage of PALSAR images is shown in Fig. 1. Taking advantage of the excellent penetration ability of L-band (wavelength = 23.6 cm), the ALOS/PALSAR data maintains an acceptable level of signal-to-noise ratio even within interferograms with long spatial and temporal baselines. However, it is challenging for Persistent Scatterer InSAR (PSInSAR) approach without any baseline limitation to obtain sufficient ground point measurements at the TVG due to small deformation magnitude and lack of pointwise scatterers [21]. Alternatively, we use short-baseline interferograms to suppress the decorrelation effect with initial baseline thresholds of 1600 m and 600 days, respectively. Then 1-arc-second SRTM DEM [22] data is applied to remove topographic contribution to the interferogram phase. The interferograms are multilooked by 3 pixels in range and 7 pixels in azimuth, resulting in a spatial resolution of approximately 20 m. To further mitigate the decorrelation noise, we estimate interferogram coherence and perform low-pass filtering by using the nonlocal filter [23]. The interferometric combinations are slimmed down based on interferogram coherence, leading to 40 interferograms remaining (Fig. 2). We further exclude the points with high noise level according to the average coherence map. The selected coherent points are then unwrapped using the minimum cost flow [24] algorithm in each interferogram. The unwrapped phases of the coherent points serve as the basic observations for the subsequent MTInSAR analysis.

B. Correction for Orbital Error and Tropospheric Delay

The MTInSAR techniques, no matter PSInSAR or small baseline subset techniques [25]−[28], have been widely applied in mapping ground surface deformation. However, the accurate retrieval of deformation is still potentially affected by abnormal phase ramps due to orbital error and atmospheric delays. For ALOS/PALSAR data, the inaccurate orbital determination at times can cause errors up to 30 cm [29]. The stratified tropospheric delays at the TVG that vary in space and time bring additional data processing challenges. In this study, we aim to address these phase ramp errors by modifying the correction methods proposed by Liang *et al*. [30] and Zhang *et al*. [31].

Considering that the troposphere exhibits variability in time and space, local estimation in predefined windows can better fit the linear relation between stratified tropospheric delays and elevation compared with the global fitting [30], [32]. In this study, we divide the interferogram scene into 8 × 8 regular patches, each of which has a spatial size of 5 × 5 km and

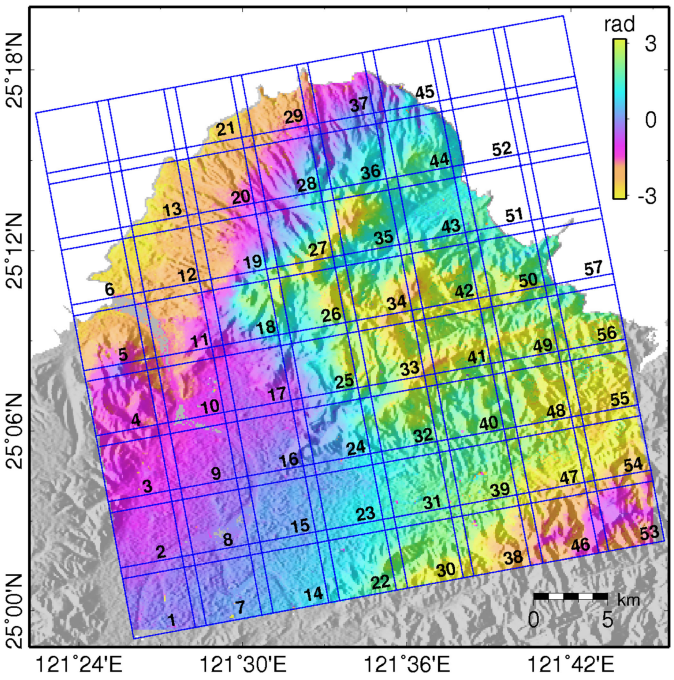

Fig. 3. Patch segmentation applied in study area. The shown interferogram corresponds to the pair 20101023-20101208.

20% overlaps to ensure consistency between adjacent patches. Because the interferogram represents the linear combination of two SAR images, in each patch, we model the phase ramp due to orbital error and stratified tropospheric delays in a SAR image as [33]

$$\phi^i_{\text{orb+trop}} = a^i_0 + a^i_1 \cdot x + a^i_1 \cdot y + a^i_2 \cdot xy + a^i_3 \cdot h \tag{1}$$

where $\phi^i_{\text{orb+trop}}$ represents the phase ramp due to orbital error and stratified tropospheric delays in ith SAR image; x and y are the coordinate indexes in the range and azimuth directions, respectively; h is the elevation; a^i_0, a^i_1, a^i_2, and a^i_3 are the unknown polynomial coefficients. The phase ramp in each patch of a given interferogram can be expressed as

$$\phi^{i,j}_{\text{orb+trop}} = \left(a^i_0 + a^i_1 \cdot x + a^i_1 \cdot y + a^i_2 \cdot xy + a^i_3 \cdot h\right) - \left(a^j_0 + a^j_1 \cdot x + a^j_1 \cdot y + a^j_2 \cdot xy + a^j_3 \cdot h\right) \tag{2}$$

where i and j are the primary and secondary SAR images. Note that the determination of the polynomial coefficients in patches is prone to the localized phase contributions, including ground deformation and topographic error. Alternatively, compared with deformation signal, orbital error and stratified tropospheric delays have a weak temporal correlation [17], [31], which can be used to separate the orbital error and stratified tropospheric delays from the deformation signal. Therefore, in each patch, we model the deformation and topographic error as follows:

$$\phi^{i,j}_{\text{defo+topo}} = -\frac{4\pi}{\lambda} \cdot \begin{bmatrix} T_{ij} & \frac{B_{\perp,ij}}{r \cdot \sin\theta} \end{bmatrix} \cdot \begin{bmatrix} v \\ \Delta h \end{bmatrix} \tag{3}$$

where $\phi^{i,j}_{\text{defo+topo}}$ represents the phase component due to deformation and topographic error within interferogram; λ is the radar wavelength; r is the slant range distance from satellite to ground surface; θ is the incident angle; T_{ij} and $B_{\perp,ij}$ are the temporal and spatial baseline of interferogram, respectively; v and Δh represent the unknown parameters of deformation rate and topographic error, respectively. Assuming that there are M interferograms formed from N SAR images and K coherent points are selected in a local patch, the relationship between the unwrapped phase observations and the phase contributions in M interferograms can be expressed by combining (2) and (3)

$$\Phi = \begin{bmatrix} B_{\text{orb+trop}} & B_{\text{defo+topo}} \end{bmatrix} \cdot \begin{bmatrix} P_{\text{orb+trop}} \\ P_{\text{defo+topo}} \end{bmatrix} + \varepsilon \tag{4}$$

where Φ represents an $(M \times K) \times 1$ vector of the unwrapped phase observations in the local patch, $B_{\text{orb+trop}}$ is an $(M \times K) \times 4(N-1)$ design matrix whose elements can be determined by the spatial coordinates and interferometric combinations; $B_{\text{defo+topo}}$ is an $(M \times K) \times 2K$ design matrix whose element is determined by the temporal and spatial baselines of interferograms; $P_{\text{orb+trop}}$ is a $4(N-1) \times 1$ vector containing unknown polynomial coefficients for $N-1$ SAR images with the coefficients of the reference SAR image being zeros; $P_{\text{defo+topo}}$ is a $2K \times 1$ vector containing deformation rate and topographic error for K points; ε represents an $(M \times K) \times 1$ phase residual vector due to the unmodeled deformation and turbulence signals. The large linear system can be solved by implementing sparse matrix factorization with the constraint of minimizing $\|\varepsilon\|^2$ [34]. After estimation of orbital error and stratified tropospheric delays, the associated phase contributions can be removed from each patch. The correction procedure is iteratively implemented in all patches. To invert the corrected patches to interferograms, we construct Delaunay network to connect the coherent points in each patch. Therefore, the corrected interferograms can be derived by integrating the phase difference from arcs to points. Note that some repetitive arcs within the overlapped areas may have unequal phase difference values. This is reasonable since the spatial variability of troposphere may cause different phase-elevation relations in different patches [30], [32]. To address this problem, we only remain the arcs with the smallest phase difference residuals that are calculated from (4) [30].

The processing flow of MTInSAR analysis with the correction of orbital error and stratified tropospheric delays is outlined in Fig. 4. Starting from the unwrapped coherent points, the interferogram is divided into regular patches with overlaps. In each patch, the orbital error and stratified tropospheric delays are parameterized by (1) and (2) while the deformation rate and topographic errors are modeled by (3). Then the overall phase contributions are jointly modeled in (4) which are solved by sparse matrix factorization. The estimated orbital error and stratified tropospheric delay are removed from the unwrapped phases in each patch. Subsequently, we construct Delaunay network in each patch and obtain the corrected interferograms by integrating the phase differences from arcs to points. In the next step, the time-series displacements can be derived based on the corrected interferograms. Since the deformation rate and topographic error have been obtained in each patch, they can be further converted to the interferogram scene along

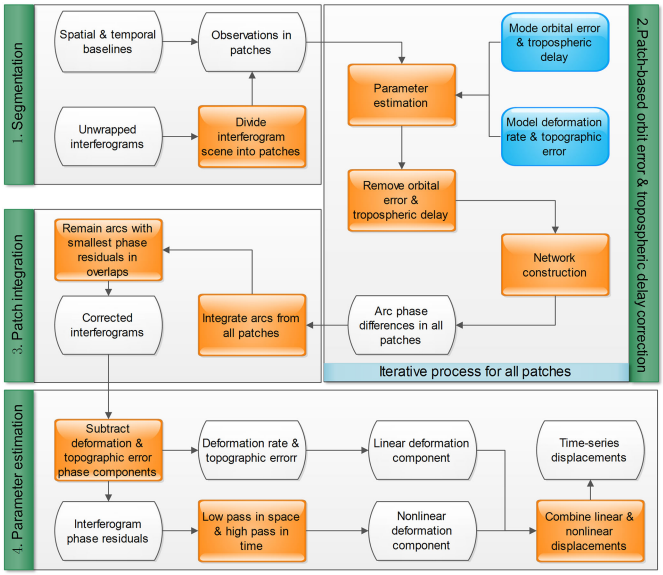

Fig. 4. Workflow diagram of time-series deformation estimation with corrections of orbital error and tropospheric delay.

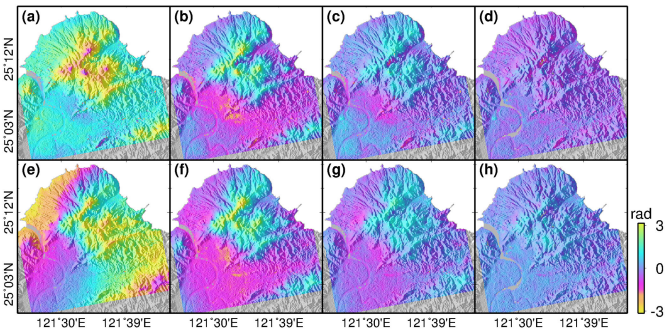

Fig. 5. Examples of phase ramp correction in interferometric pairs (a)–(d) 20100723-20101208 and (e)–(h) 20101023-20101208. (a) and (e) Original interferograms before phase ramp correction. (b) and (f) Interferograms after global correction for orbital error. (c) and (g) Interferograms after global correction for orbital error and tropospheric delay. (d) and (h) Interferograms after patch-based correction for orbital error and tropospheric delay.

with patch combination. We further subtract the deformation rate and topographic error components from the interferogram after phase ramp correction. The resulted phase residual maps mainly contain nonlinear deformation and turbulent artifacts. To mitigate the effect of turbulent artifacts, it is necessary to perform filtering operation on the phase residuals [25]−[28]. In this case, a spatial and temporal filter proposed in PSInSAR approach is applied on phase residuals [28]. Once the phase residuals are filtered, the final time-series displacement can be derived by combining the linear deformation signal with the nonlinear displacements.

III. Results and Discussions

A. Orbital Error and Stratified Tropospheric Delay Correction

Fig. 5(a) and (e) presents two typical interferograms generated from pairs 20100723-20101208 and 20101023-20101208. It can be seen that the phase variation in pair 20100723-20101208 [Fig. 5(a)] has a high correlation with topography, while the pair 20101023-20101208 [Fig. 5(e)] is dominated by global trend and local phase ramp in mountainous area, indicating that the interferograms suffer from orbital error and stratified tropospheric delays. To correct the phase ramps, we apply the proposed correction method on the interferograms. Fig. 5(d) and (h) shows the interferograms corrected by the proposed method. As a comparison, we also apply the conventional methods to correct the phase ramps. Fig. 5(b) and (f) displays the corrected interferograms through globally estimating orbital error, and Fig. 5(c) and (g) corresponds to the results of globally corrected orbital error and tropospheric delays. As expected, apparent elevation-dependent phase ramps remain in mountainous area [Fig. 5(b) and (c)] due to the lack of correction of stratified tropospheric delays. In Fig. 5(c) and (g), although the tropospheric delays have been mitigated by a global linear fitting, the spatial variation of troposphere degrades the correction performance, resulting in phase residual ramp in mountainous area. Alternatively, by implementing the proposed joint estimation in the local patches, the phase ramps due to orbital error and tropospheric delays are well corrected despite the presence of spatial variability of troposphere and confounding signals. The results suggest that the proposed method can improve the correction of orbital error and stratified tropospheric delays, which is vital for the subsequent time-series displacement retrieval.

B. Comparison With GPS Measurements

In order to validate the accuracy of InSAR measurements, we compare InSAR time-series displacements with GPS displacements obtained from the Institute of Earth Science of Academia Sinica. Before comparison, we isolate localized deformation signal from the tectonic movement in the northern Taiwan. We select a far-field GPS site with stable time-series displacement as the reference site (i.e., taip). The displacements of other GPS sites are calibrated with respect to the reference site. The 3-D displacements of GPS measurements are then projected into the LOS direction of InSAR data. A total of 20 GPS stations (shown in Fig. 1) that have overlapping observations with InSAR for more than three years are selected to evaluate the accuracy of time-series displacement measurement in InSAR. As can be seen, InSAR time-series displacements have good agreement with GPS measurements, both of which exhibit an annual oscillation and a gradual trend. The uncertainties of most InSAR measurements are smaller than 5 mm. The standard deviation (STD) of misfit between InSAR and GPS ranges from 2.1 to 8.8 mm. Although some transient deformation signals in GPS measurements are omitted by the InSAR data (e.g., tans), this is resulted from limited availability of SAR data in 2009. In general, most of the differences between InSAR and GPS results are within the InSAR error bars, confirming the reliability of our InSAR measurements.

C. Spatial Pattern and Temporal Behavior of Movement

Benefiting from the aforementioned time-series processing, the deformation measurements at the TVG appear in a dense spatial extent. Fig. 7 shows the deformation rate map at the TVG

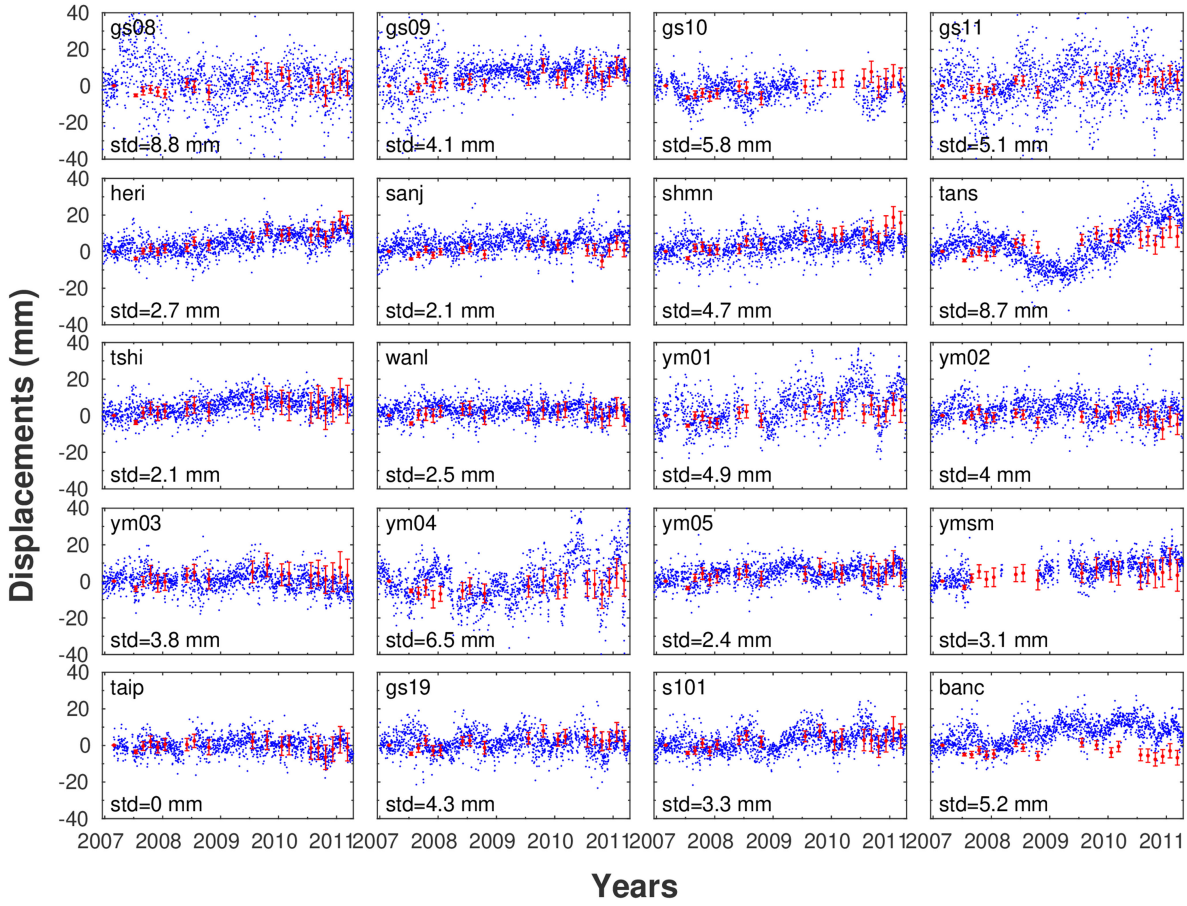

Fig. 6. Comparison of the time-series displacements of InSAR (red dots with error bars) and 20 GPS stations (blue dots). The error bar of the InSAR displacement represents the standard deviation which is estimated within 1 km around GPS site.

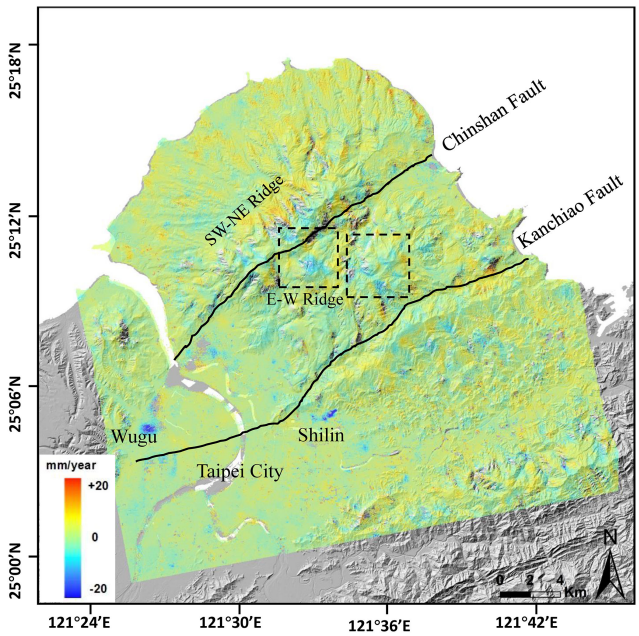

Fig. 7. Average deformation velocity map line-of-sight (LOS) direction over the TVG. The black solid lines indicate the fault traces by morphological evidence. The black dashed boxes indicate the areas that are further analyzed in the temporal behaviors.

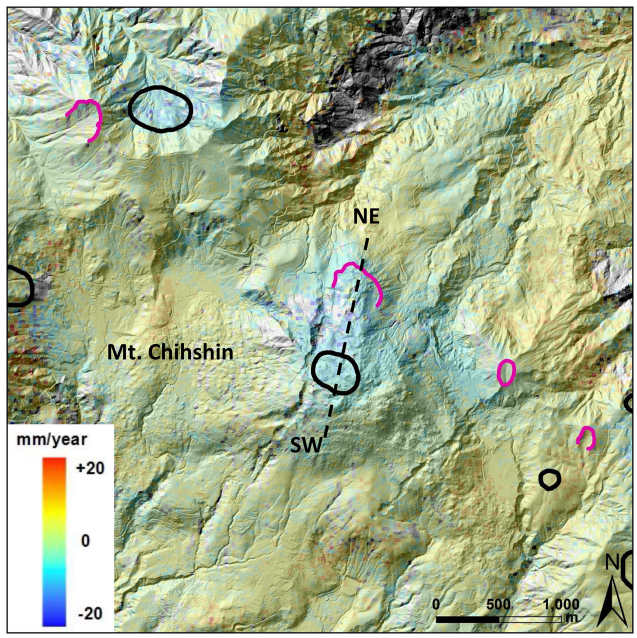

Fig. 8. Average LOS deformation velocity map over Mt. Chihshin. The black and magenta lines show the outlines of crater and inferred cater, respectively. The black dashed line marks the location of displacement profile shown in Fig. 9.

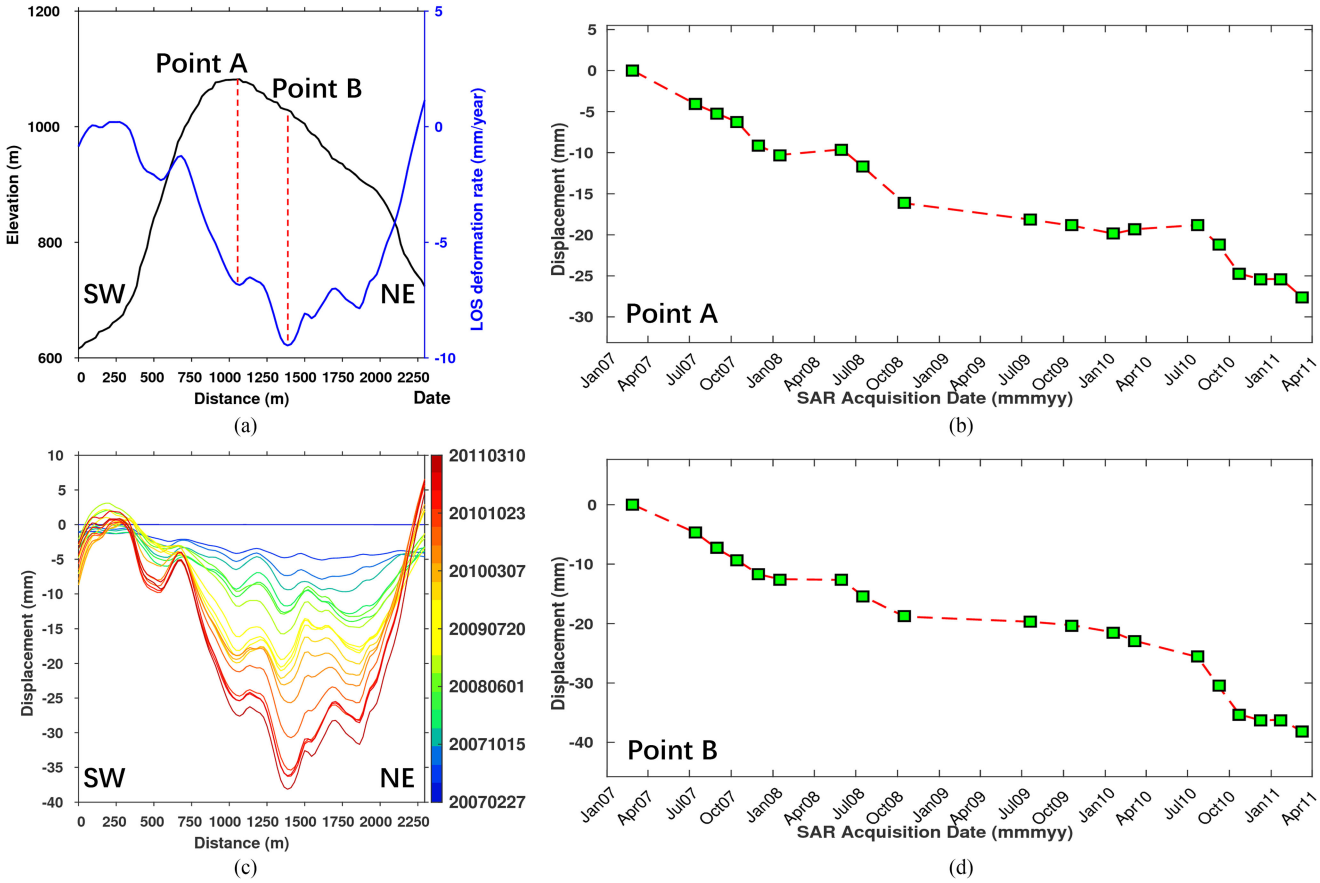

Fig. 9. (a) Profile of elevation and mean LOS deformation velocity at Mt. Chihshin. (b) Cumulative displacement of Point A. (c) Profile of time-series displacement at Mt. Chihshin. (d) Cumulative displacement of Point B. The location of profile is indicated in Fig. 8.

during the investigation period. An uplift of about 10 mm/year in LOS direction is detected at the SW-NE volcanic ridge. The uplift distribution is consistent with the results from Envisat data by PSInSAR technique [21]. Considering the Chinshan Fault as a boundary, the uplift at the SW-NE ridge might be controlled by the post-collision extensional tectonic regime [2], [21], [35]. By contrast, subsidence of approximately 10 mm/year is identified at E-W volcanic ridge, which consists of numerous well-preserved volcanic features [36]. This is reasonable because the land surface temperature at E-W ridge is higher than that at the SW-NE ridge due to strong fumarolic activities. This indicates that the subsidence at E-W ridge might be caused by enhanced hydrothermal circulation at depth, probably related to tectono-magmatic activity [37], [38]. In addition to the ground movement pattern at the TVG, two isolated subsidence areas are identified in Taipei Basin, where the average velocity reaches 20 mm/year. Since the study focuses on analyzing the deformation condition at the TVG, we further explore the temporal behaviors of movements that are enclosed by the dashed boxes, i.e., Mts. Chihshin and Huangzuei volcano subgroups.

As the youngest volcano at the TVG, Mt. Chihshin has the most well-preserved edifice. It has the highest summit at the TVG with an elevation of 1120 m. Because the last phreatic explosion occurred near Mt. Chihshin about 6000 years ago, Mt. Chihshin is considered to be potentially active in recent

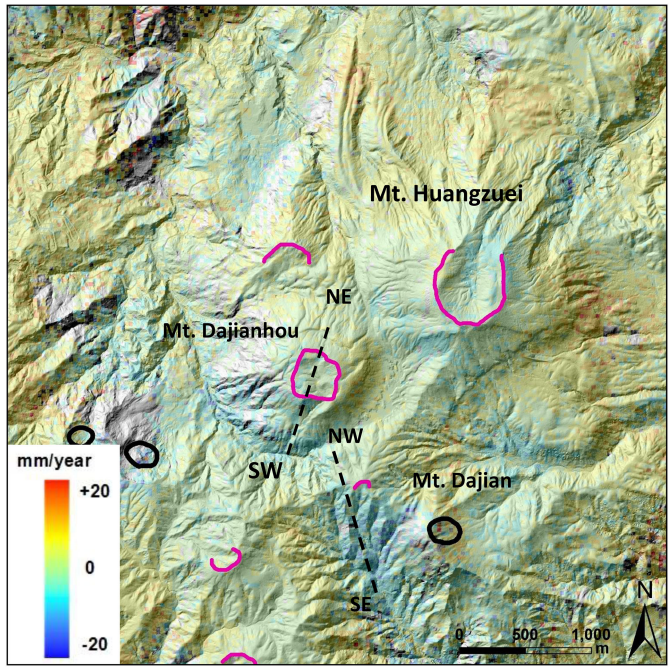

Fig. 10. Average LOS deformation velocity map over Mts. Huangzuei, Dajianhou, and Dajian. The black and magenta lines show the outlines of crater and inferred cater, respectively. The black dashed lines mark the location of displacement profiles shown in Fig. 11.

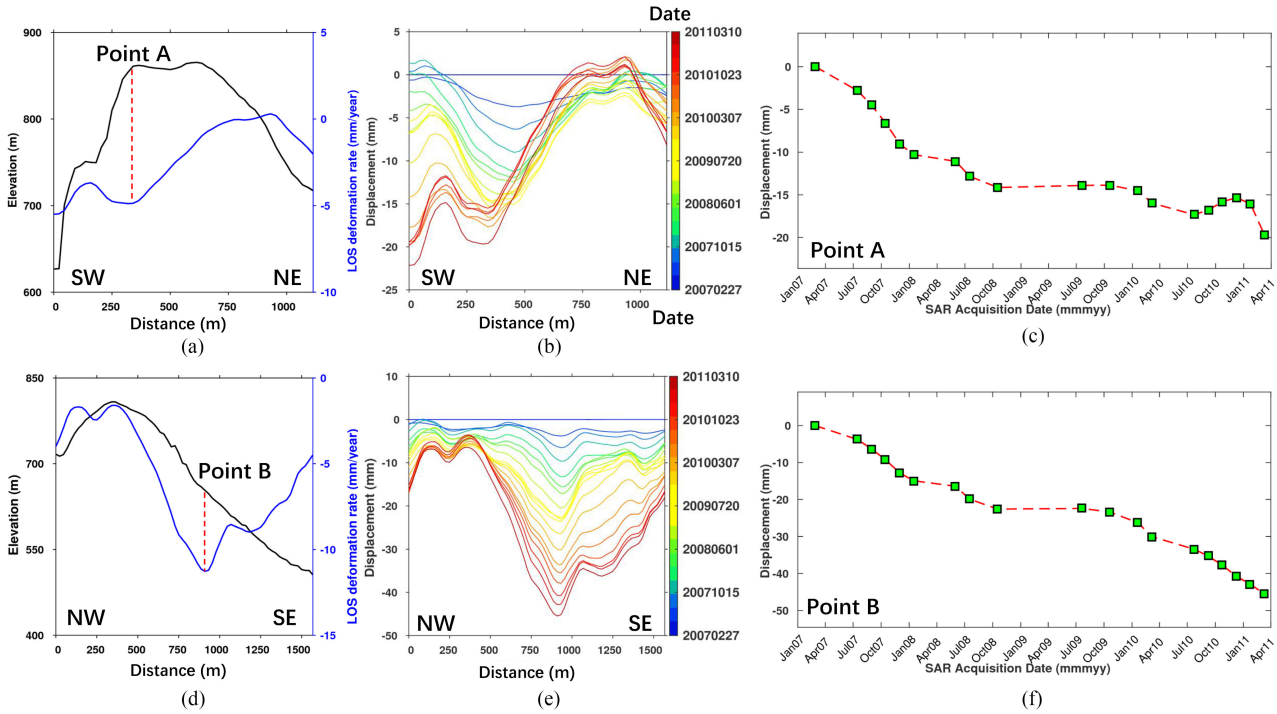

Fig. 11. (a) Profile of elevation and mean LOS deformation velocity at Mt. Dajianhou. (b) Profile of time-series displacement at Mt. Dajianhou. (c) Cumulative displacement of Point A. (d) Profile of elevation and mean LOS deformation velocity along Mt. Dajian. (e) Profile of time-series displacement along Mt. Dajian. (f) Cumulative displacement of Point B.

years [4]. In Fig. 8, the SW-NE volcanic ridge of Mt. Chihshin is parallel with the volcanic lineament, where volcanic morphological feature is observed on the east of the crater and caldera. This implies an extension caused by tectono-magmatic activity as evidenced by geochemistry analysis [6]. It also tells that the deformation mechanism is relative to the subsidence pattern. Fig. 9 presents the displacements of Point A (crater) and Point B (caldera) on the volcanic ridge, which is approximately 2300 m with an elevation change of about 520 m. The figure indicates that the deformation mechanism of both points is relative to the subsidence pattern at a maximum rate of −9 mm/year in the LOS direction over Mt. Chihshin. We further visualize the spatial and temporal patterns of the volcanic ridge, where the cumulative displacement indicates consistent deformation rate and subsidence pattern between February 27, 2007 and March 10, 2011 [Fig. 9(b)]. From the time-series displacements of Point A and Point B [Fig. 9(c) and (f)], we further notice that both points have a rather persistent trend, despite the fact that the deformation rate of Point B is relatively larger with a maximum displacement of −40 mm. This phenomenon is consistent with the repeated leveling results, indicating a possible relation between subsidence and magma activity beneath the Earth's surface [9], [10], [15]. Furthermore, as InSAR time-series data provide information on the slow-motion collapse, a creeping is therefore observed on the NW flank of Mt. Chihshin, suggesting an ongoing mass removal process from the magma chamber. This process, also known as postvolcanic action, such as fumarole, sulfur fume, and hot spring, can trigger a hydrothermal eruption as surface water is stored in and flows through fractures. This indicates that the observed subsidence is likely caused by the decompression of water due to mass removal process, which can possibly result in a hydrothermal eruption in the future [38].

Mt. Huangzuei volcano subgroup is located at the east of Mt. Chihshin. Fig. 10 shows the mean deformation map over this area. The results indicate that the summit of SE flank has undergone small subsidence during the investigation period. Although the motion in Mt. Huangzuei is not significant, it is still worth noting since it has the best-preserved volcanic crater at the TVG [39]. In addition, two persistent subsiding areas are identified at two young volcanoes, i.e., Mts. Dajian and Dajianhou. The subsidence of both volcanoes concentrates at the southern flanks of main bodies. We extract the profiles of the average deformation rate and cumulative displacements from two volcanoes (Fig. 11). The profiles extend from SW to NE and from NW to SE, respectively. We further find that, in Mt. Dajianhou, the subsidence mainly occurs at the SW flank, while the subsidence in Mt. Dajian is distributed at the SE flank. Although two subsidence patterns vary in magnitude, they present similar temporal deformation changes that constantly move down following an acceleration after July 2010. We further calculate the correlation coefficient of the cumulative displacements between Mts. Chihshin and Huangzuei. The results show that the correlation values are 0.99 between Mts. Chihshin and Dajian and 0.91 between Mts. Chihshin and Dajianhou. According to the precise leveling surveys [38], a deflation source was obtained at approximately 0.5 km northeast of Mt. Chihshin. We consider that the subsidence at Mts. Chihshin and Huangzuei represents the same response of released hydrothermal fluid at a constant rate from 2007 to 2010 with a slight acceleration after July 2010.

IV. Conclusion

Whether the TVG contains active volcanoes has been debated for decades. Recent analysis from seismological, geophysical, and geochemical observations suggests that the volcano-hydrothermal activity is still significant at the TVG. The increasing concern about the eruption potential necessitates an urgent need for in-depth investigation toward the status of TVG. In this study, we adopted an improved MTInSAR approach to investigate the spatial and temporal deformation involved in volcano-hydrothermal activities in this area. The stratified atmospheric delays and orbit error were corrected by applying a patch-based joint model. The comparison with independent GPS data validated the derived deformation measurement with an uncertainty of around 5 mm. The spatial deformation patterns indicate an uplift of 10 mm/year at the SW-NE ridge and subsidence with a rate of 10 mm/year at the E-W ridge. The temporal deformation variations at Mts. Chihshin and Huangzuei have demonstrated the occurrence of subsidence at a constant speed in the period 2007−2010 and a slight acceleration after July 2010. Although the subsidence magnitudes varied at two volcano subgroups, they exhibited similar time-series changes with the correlation coefficients of 0.9 above. This indicated that the subsidence at Mts. Chihshin and Huangzuei may have the same cause of released hydrothermal fluid driven by a crustal magma reservoir at depth.

Acknowledgment

The authors would like to thank the Japan Aerospace Exploration Agency (JAXA) for providing the ALOS/PALSAR data via Project ER2A2N045 and 3381, Dr. Ya-Ju, Hsu from Institute of Earth Sciences, Academic Sinica for providing the continuous GPS data, and Dr. Thor Hansteen for his constructive suggestions.

References

[1] K.-H. Kim, C.-H. Chang, K.-F. Ma, and J.-M. C. K.-C. Chen, "Modern seismic observations in the Tatun volcano region of northern Taiwan: Seismic/volcanic hazard adjacent to the Taipei metropolitan area," *Terr. Atmos. Ocean. Sci.*, vol. 16, no. 3, pp. 579–594, 2005.

[2] L. S. Teng, "Extensional collapse of the northern Taiwan mountain belt," *Geology*, vol. 24, no. 10, pp. 949–952, 1996.

[3] S. Song, T. Yang, Y. Yeh, S. Tsao, and H. Lo, "The Tatun volcano group is active or extinct?," *J. Geological Soc. China*, vol. 43, no. 3, pp. 521–534, 2000.

[4] A. Belousov, M. Belousova, C.-H. Chen, and G. F. Zellmer, "Deposits, character and timing of recent eruptions and gravitational collapses in Tatun volcanic group, northern Taiwan: Hazard-related issues," *J. Volcanol. Geothermal Res.*, vol. 191, no. 3, pp. 205–221, 2010.

[5] A. Szakács, "Redefining active volcanoes: A discussion," *Bull. Volcanol.*, vol. 56, no. 5, pp. 321–325, 1994.

[6] T. Yang, Y. Sano, and S. Song, "3He/4He ratios of fumaroles and bubbling gases of hot springs in Tatun Volcano Group, north Taiwan," *Nuovo Cimento-Soc. Ital. Di Fisica Sezione C*, vol. 22, pp. 281–286, 1999.

[7] C. H. Lin, "Evidence for a magma reservoir beneath the Taipei metropolis of Taiwan from both S-wave shadows and P-wave delays," *Sci. Rep.*, vol. 6, Dec. 2016, Art. no. 39500.

[8] K. I. Konstantinou, C.-H. Lin, and W.-T. Liang, "Seismicity characteristics of a potentially active quaternary volcano: The Tatun Volcano Group, northern Taiwan," *J. Volcanol. Geothermal Res.*, vol. 160, no. 3-4, pp. 300–318, 2007.

[9] K. I. Konstantinou, C. H. Lin, W. T. Liang, and Y. C. Chan, "Seismogenic stress field beneath the Tatun Volcano Group, northern Taiwan," *J. Volcanol. Geothermal Res.*, vol. 187, no. 3-4, pp. 261–271, 2009.

[10] C. H. Lin *et al.*, "Preliminary analysis of volcanoseismic signals recorded at the Tatun Volcano Group, northern Taiwan," *Geophys. Res. Lett.*, vol. 32, no. 10, 2005, Art. no. L10313.

[11] H.-Y. Wen *et al.*, "Soil CO_2 flux in hydrothermal areas of the Tatun volcano group, northern Taiwan," *J. Volcanol. Geothermal Res.*, vol. 321, pp. 114–124, 2016.

[12] H. Lee, T. F. Yang, T. F. Lan, S. Song, and S. Tsao, "Fumarolic gas composition of the Tatun volcano group, northern Taiwan," *Terr. Atmos. Ocean. Sci.*, vol. 16, no. 4, 2005, Art. no. 843.

[13] T. Wang, K. DeGrandpre, Z. Lu, and J. T. Freymueller, "Complex surface deformation of Akutan volcano, Alaska revealed from InSAR time series," *Int. J. Appl. Earth Observation Geoinformation*, vol. 64, pp. 171–180, 2018.

[14] Z. Lu and D. Dzurisin, *InSAR Imaging of Aleutian Volcanoes: Monitoring a Volcanic Arc from Space (Geophysical Sciences)*. Vienna, Austria: Springer-Verlag Berlin Heidelberg, 2014.

[15] M. Murase, C.-H. Lin, F. Kimata, H. Mori, and H.-C. Pu, "Volcano-hydrothermal activity detected by precise levelling surveys at the Tatun volcano group in northern Taiwan during 2006–2013," *J. Volcanol. Geothermal Res.*, vol. 286, pp. 30–40, 2014.

[16] Y.-J. Hsu, S.-B. Yu, M. Simons, L.-C. Kuo, and H.-Y. Chen, "Interseismic crustal deformation in the Taiwan plate boundary zone revealed by GPS observations, seismicity, and earthquake focal mechanisms," *Tectonophysics*, vol. 479, no. 1, pp. 4–18, 2009.

[17] J. Biggs *et al.*, "The postseismic response to the 2002 m 7.9 Denali fault earthquake: Constraints from InSAR 2003–2005," *Geophysical J. Int.*, vol. 176, no. 2, pp. 353–367, 2009.

[18] J. J. Mohr, N. Reeh, and S. N. Madsen, "Three-dimensional glacial flow and surface elevation measured with radar interferometry," *Nature*, vol. 391, no. 6664, pp. 273–276, 1998.

[19] H. Liang *et al.*, "Investigation of slow-moving artificial slope failure with multi-temporal InSAR by combining persistent and distributed scatterers: A case study in northern Taiwan," *Remote Sens.*, vol. 12, no. 15, 2020, Art. no. 2403.

[20] F. Qu *et al.*, "Mapping ground deformation over Houston–Galveston, Texas using multi-temporal InSAR," *Remote Sens. Environ.*, vol. 169, pp. 290–306, 2015.

[21] C.-P. Chang *et al.*, "Monitoring of surface deformation in northern Taiwan using DInSAR and PSInSAR techniques," *Terr., Atmos. Ocean. Sci.*, vol. 21, no. 3, pp. 447–461, 2010.

[22] T. G. Farr *et al.*, "The shuttle radar topography mission," *Rev. Geophys.*, vol. 45, no. 2, 2007, Art. no. RG2004.

[23] C.-A. Deledalle, L. Denis, F. Tupin, A. Reigber, and M. Jäger, "NL-SAR: A unified nonlocal framework for resolution-preserving (Pol)(In) SAR denoising," *IEEE Trans. Geosci. Remote Sens.*, vol. 53, no. 4, pp. 2021–2038, Apr. 2015.

[24] M. Costantini, "A novel phase unwrapping method based on network programming," *IEEE Trans. Geosci. Remote Sens.*, vol. 36, no. 3, pp. 813–821, May 1998.

[25] L. Zhang, Z. Lu, X. Ding, H.-S. Jung, G. Feng, and C.-W. Lee, "Mapping ground surface deformation using temporarily coherent point SAR interferometry: Application to Los Angeles basin," *Remote Sens. Environ.*, vol. 117, pp. 429–439, 2012.

[26] A. Hooper, P. Segall, and H. Zebker, "Persistent scatterer interferometric synthetic aperture radar for crustal deformation analysis, with application to Volcán Alcedo, Galápagos," *J. Geophys. Res.*, vol. 112, no. B7, 2007, Art. no. B07407.

[27] P. Berardino, G. Fornaro, R. Lanari, and E. Sansosti, "A new algorithm for surface deformation monitoring based on small baseline differential SAR interferograms," *IEEE Trans. Geosci. Remote Sens.*, vol. 40, no. 11, pp. 2375–2383, Nov. 2002.

[28] A. Ferretti, C. Prati, and F. Rocca, "Permanent scatterers in SAR interferometry," *IEEE Trans. Geosci. Remote Sens.*, vol. 39, no. 1, pp. 8–20, Jan. 2001.

[29] R. Nakamura, S. Nakamura, N. Kudo, and S. Katagiri, "Precise orbit determination for ALOS," in *Proc. 20th Int. Symp. Space Flight Dyn.*, vol. 23, no. 1, pp. 14–19, 2007.

[30] H. Liang, L. Zhang, X. Ding, Z. Lu, and X. Li, "Toward mitigating stratified tropospheric delays in multitemporal InSAR: A quadtree aided joint model," *IEEE Trans. Geosci. Remote Sens.*, vol. 57, no. 1, pp. 291–303, Jan. 2019.

[31] L. Zhang, X. Ding, Z. Lu, H.-S. Jung, J. Hu, and G. Feng, "A novel multitemporal InSAR model for joint estimation of deformation rates and orbital errors," *IEEE Trans. Geosci. Remote Sens.*, vol. 52, no. 6, pp. 3529–3540, Jun. 2014.
[32] D. Bekaert, A. Hooper, and T. Wright, "A spatially variable power law tropospheric correction technique for InSAR data," *J. Geophys. Res., Solid Earth*, vol. 120, no. 2, pp. 1345–1356, 2015.
[33] Q. Sun, L. Zhang, X. Ding, J. Hu, Z. Li, and J. Zhu, "Slope deformation prior to Zhouqu, China landslide from InSAR time series analysis," *Remote Sens. Environ.*, vol. 156, pp. 45–57, 2015.
[34] D. C.-L. Fong and M. Saunders, "LSMR: An iterative algorithm for sparse least-squares problems," *SIAM J. Sci. Comput.*, vol. 33, no. 5, pp. 2950–2971, 2011.
[35] L. S. Teng, "Tectonic aspects of the Paleogene depositional basin of northern Taiwan," *Proc. Geological Soc. China*, vol. 34, no. 4, pp. 313–335, 1991.
[36] C. C. Yang, J. K. Liu, M. T. Huang, and W. S. Chen, "DTM for mapping the volcanic landforms of Tatun volcano group in northern Taiwan," *J. Photogrammetry Remote Sens.*, vol. 9, no. 2, pp. 1–8, 2004.
[37] H.-P. Chan, C.-P. Chang, T.-H. Lin, M. Blackett, H. Kuo-Chen, and A. T.-S. Lin, "The potential of satellite remote sensing for monitoring the onset of volcanic activity on Taipei's doorstep," *Int. J. Remote Sens.*, vol. 41, no. 4, pp. 1372–1388, 2020.
[38] A. Nurmawati and K. I. Konstantinou, "Hazard assessment of volcanic ballistic impacts at Mt Chihshin, Tatun volcano group, northern Taiwan," *Nat. Hazards*, vol. 92, no. 1, pp. 77–92, 2018.
[39] Y.-M. Lai, Y.-J. Lin, S.-R. Song, Y.-W. Tsai, Y.-C. Hsieh, and W. Lo, "Topography and volcanology of the Huangtsuishan volcano subgroup, northern Taiwan," *Terr., Atmos. Ocean. Sci.*, vol. 21, no. 3, pp. 599–609, 2010.

Hongyu Liang (Member, IEEE) was born in Bazhong, China, in 1991. He received the M.Sc. degree in geomatics and the Ph.D. degree in geodesy and geodynamics from The Hong Kong Polytechnic University, Kowloon, Hong Kong, China, in 2014 and 2020, respectively.

He has been an Assistant Professor with the College of Surveying and Geo-Informatics, Tongji University, Shanghai, China, since 2021. His research interests include estimation theory and advanced processing developments for multitemporal SAR interferometry and deformation monitoring.

Xin Li was born in Tai'an, Shandong, China, in 1990. She received the B.S. degree in geography information science from the Shandong University of Science and Technology, Qingdao, China, in 2012, and the M.S. degree in geoinformation science from The Chinese University of Hong Kong (CUHK), Hong Kong, in 2013.

She is with State Key Laboratory of Resources and Environmental Information System, Institute of Geographic Sciences and Natural Resources Research, Chinese Academy of Sciences, Beijing, China. Her research interests include the atmospheric remote sensing application and spatial–temporal analysis.

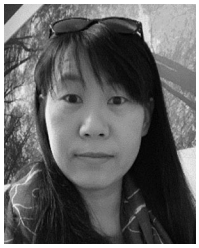

Rou-Fei Chen was born in Taipei, Taiwan, in 1974. She received the Ph.D. degree in geosciences (major in structural geology and tectonics) from Université Pierre et Marie Curie, Paris, France, in 2005. Her Ph.D. thesis was focused on surface process analysis investigation of neotectonics effects and morphological evolution of western Taiwan.

She has been an Associate Professor with the Department of Geology, Chinese Culture University, Taipei, Taiwan, since 2018. She is currently an Assistant Professor with Department of Materials and Mineral Resources Engineering, National Taipei University of Technology, Taipei, Taiwan. Her current research focuses on applications of remote sensing data in natural hazard and disaster management.